



Influence of Friction Stir Weld Seam Distribution on Spun Formed Workpieces

Shouyi Sun¹ · Jin Wang¹ · Bo Gao¹ · Gaowei Cao¹ · Shuai Zhang¹

Received: 23 October 2023 / Revised: 28 February 2024 / Accepted: 5 March 2024 / Published online: 2 April 2024
© The Author(s), under exclusive licence to Korean Society for Precision Engineering 2024

Abstract

Employing friction stir welding (FSW) technology to join small plate blanks into larger ones, followed by a spinning process, adeptly surpasses the dimensional constraints of traditionally rolled plate blanks. This innovative approach paves the way for the fabrication of large and super-sized thin-walled rotary components, with significant implications in the aerospace sector. In this methodology, the number and layout of welds critically influence the precision of forming in spun workpieces, which could be pivotal in the success of spun tailor-welded blanks (TWBs). Consequently, dedicated experimental research into the spin forming of TWBs, varying in weld numbers and configurations, is essential. This investigation employed annealed 2195 Al–Li alloy plates as the material for experimentation. Four types of blanks with varying weld distributions and increasing weld numbers were designed, prepared through multiple FSW processes, followed by spinning. Comprehensive measurements of weld torsion angles, surface morphology, thickness variations, and forming accuracy of the workpieces post-spinning were conducted. The results show that with the increase of the number of welds, the weld torsion angle of the workpiece after spinning decreases. The spinning process can significantly reduce the surface morphology of the weld area. The thickness of the weld area is thinner than that of the non-weld area, and the superposition of the welds will aggravate the thickness reduction. In addition, the accuracy deviation of the workpiece mainly occurs in the initial and final stages of spinning forming. A negative accuracy deviation occurs at the beginning of the spinning, and a positive accuracy deviation is observed at the end of the spinning stage. In the spinning stage, the welding area appears slight bulge. As the number of welding seams increases, the accuracy of the workpiece decreases.

Keywords Spin forming · Friction stir welding · Aluminum lithium alloy · Tailor-welded blanks · Accuracy

1 Introduction

Thin-walled, complexly curved surface components are extensively used in advanced aircraft, spacecraft, and related fields. The spinning process, a sophisticated near-net shape forming method, is now widely used in manufacturing the bottoms of launch vehicle tanks and the tops of large tank bottoms. With the increased load capacity of aerospace equipment, there is a pressing demand for large-diameter, thin-walled, complexly curved parts [1, 2]. However, the direct rolling of such large, high-quality integral billets is challenging. An alternative approach involves indirectly obtaining large-scale integral plates using FSW technology,

followed by the fabrication of large-scale head parts via the spinning forming process [3–5].

To meet the application demands in the aerospace sector, aluminum-based lightweight alloys [6–9], particularly aluminum–lithium alloys, have garnered widespread attention. FSW offers a convenient method to weld small-sized aluminum–lithium alloy sheets into larger ones. Zhang et al. [10] employed FSW on 2195-T8 aluminum–lithium alloy, leading to a notable decrease in strength and plasticity of the welded joints. The strength and plasticity of the joints were reduced to 65% and 54% of the base metal, respectively. Tao et al. [11] experimented with air-cooled and water-cooled conditions in the FSW of 2198-T8 aluminum–lithium alloy. They found that the microhardness of the heat-affected zone (HAZ) was lowest under air-cooled conditions, while water cooling did not significantly alter the strength and microhardness of the weld area.

✉ Jin Wang
wangjin@qut.edu.cn

¹ School of Mechanical and Automotive Engineering,
Qingdao University of Technology, Qingdao 266525, China

To achieve improved welding performance, various auxiliary methods have been implemented in FSW. Amin et al. [12, 13] investigated the impact of vibration and cooling medium in the FSW of 5083Al alloy. They compared the effects of CO₂ laser welding, FSW, and friction stir vibration welding on the mechanical properties and formability of the developed TWBs. Mahmoud et al. [14] studied the strength and ductility of underwater FSW and friction stir vibration welding processed samples are higher than those of the FSW processed sample, and the highest strength and ductility are obtained for underwater FSW processed samples. The underwater FSW and friction stir vibration welding processed samples exhibit about 25% and 10% higher tensile strength compared to the FSW processed sample. Additionally, the corrosion resistance of FSW joints has been receiving increasing attention. Hammood et al. [15] studied the effects of FSW parameters on the corrosion performance of 2101 lean duplex stainless steel (LDSS) in simulated body fluid (SBF). The results indicated that increasing the rotational speed of the stirring needle could enhance the corrosion resistance of the joint. Laska et al. [16] investigated the corrosion performance of friction stir welded dissimilar aluminum alloys AA6082 and AA6060, as well as the parent materials, in seawater. They found that the welds exhibited higher corrosion resistance compared to the parent materials.

Spinning, particularly die-less spinning, is especially suitable for manufacturing large and extra-large thin-walled rotational body components. Lin et al. [17] proposed an edge-constrained die-less spinning process for manufacturing wrinkle-free thin-walled ellipsoid heads. They found that during the one-pass spinning process, wall thickness accuracy decreases with an increase in the forming angle or the roller fillet radius. Additionally, accuracy initially increases and then decreases with an increasing feed ratio. Yan et al. [18] analyzed the quantitative dependence of the initial forming state on the diameter of the blank and the diameter of the spinning wheel, and established the corresponding initial forming state criterion, revealing the influence of forming parameters such as blank parameters, mold parameters, and process parameters on the initial forming state criterion of die-less spinning. Zhou et al. [19] analyzed the stress and strain state of the material during the die-less spinning by building a finite element model. The wall angle, wall thickness and sheet diameter had a greater effect on the material thinning, while the rotational speed and corner radius had a smaller effect. Material thinning occurs mainly in the pre-forming stage, and whether the material continues to thin during the forming stage depends on the diameter of the sheet. Izadpanah et al. [20] used a 3D finite element model to simulate the stress, strain, and wall thickness distribution of hemispherical workpieces formed by spinning, with

the simulation results showing good agreement with the experimental outcomes.

Zhang et al. [21–23] conducted a systematic study on the spin forming of 2195 aluminum–lithium alloy plates using single-seam FSW. They discovered that the weld seam undergoes movement during the spinning process, with the direction of movement aligning with the rotation direction of the spindle. Following spinning, the average microhardness of the weld area increased by 21%, the yield strength increased by over 60%, and the tensile strength increased by more than 12% [21]. The torsion angle of the weld increases as the radius of the roller nose increases. In the horizontal direction of the workpiece, both the surface roughness of the base metal and the surface roughness of the weld are significantly improved [22]. The study proposes a multi-pass roller path scheme. The proposed multi-pass roller path scheme increases the forming height of the workpiece by 18% to 145.7 mm, resulting in improved overall forming quality [23].

In the above literatures, joining small-sized sheets into larger ones via FSW for spin forming is a viable approach to manufacturing large and extra-large thin-walled rotational body components. To enhance the microstructure and properties of the weld, auxiliary methods such as underwater welding and ultrasonics can be employed. Additionally, the spin forming of aluminum–lithium alloy with a single weld seam has been accomplished. However, to fabricate larger components, obtaining larger-sized plate blanks through multiple welding processes is essential. The distribution of weld seams critically influences the feasibility of subsequent spin forming, which has not been extensively explored in current research. In this paper, four types of blanks with varying weld seam distributions prepared by FSW were processed by spinning. Furthermore, experimental investigations revealed the influence of the quantity and distribution of weld seams on the torsion angle, surface morphology, thickness variation, and forming accuracy of the workpieces after spin forming.

2 Experimental Materials and Methods

The experiments were conducted using fully annealed 2195 Al–Li alloy plates with the thickness of 2 mm. Table 1 displays the chemical composition of the 2195 Al–Li alloy.

The welding experiments utilized the HT-JC6×8/2 FSW machine (illustrated in Fig. 1a), manufactured by Aerospace Engineering Equipment Co., Ltd. Welding was performed in the form of a butt joint. The shoulder diameter of the stirring head is 10 mm, and the length of the stirring pin is 1.7 mm. The morphology of the stirring head is shown in Fig. 1b, and the welding process is depicted in Fig. 1c. The welding parameters were as follows: the stirring head operated at a

speed of 1600 mm/r, with a feed speed of 150 mm/min, and a pressing depth of 0.2 mm.

Four distinct distribution of weld seams were designed, with their respective welding processes illustrated in Fig. 2. FSW was employed to join blanks of various shapes and quantities, each 2 mm thick, into 160 mm × 160 mm square blanks. Figure 2a shows the first type of weld seam, where two 160 mm × 80 mm rectangular blanks were fused into a square blank, featuring a single “–” shaped weld seam. Figure 2b illustrates the second type of weld seams. Initially, four 80 mm × 80 mm square blanks were joined to form two

160 mm × 80 mm rectangular blanks. Subsequently, these two blanks were combined into a single 160 mm × 160 mm square blank, featuring “+” shaped weld seams. Figure 2c presents the third type of weld seams. Initially, six 80 mm × 53.3 mm square blanks were fused into two 160 mm × 80 mm rectangular blanks. These were then joined to form a single 160 mm × 160 mm square blank, characterized by weld seams in a “±” shape. Figure 2d demonstrates the fourth type of weld seams. Initially, eight right-angled triangle blanks, each with two sides measuring 80 mm, were welded into four 80 mm × 80 mm squares. These squares

Table 1 Chemical composition of 2195 Al–Li alloy (wt.%)

Element	Si	Fe	Cu	Mn	Li	Zr	Zn	Ti	Mg
Content	0.09	0.12	4.12	0.06	0.81	0.08	0.02	0.04	0.26

Fig. 1 Joining equipment, tool, and processes: **a** FSW machine, **b** the stirring head, **c** welding process

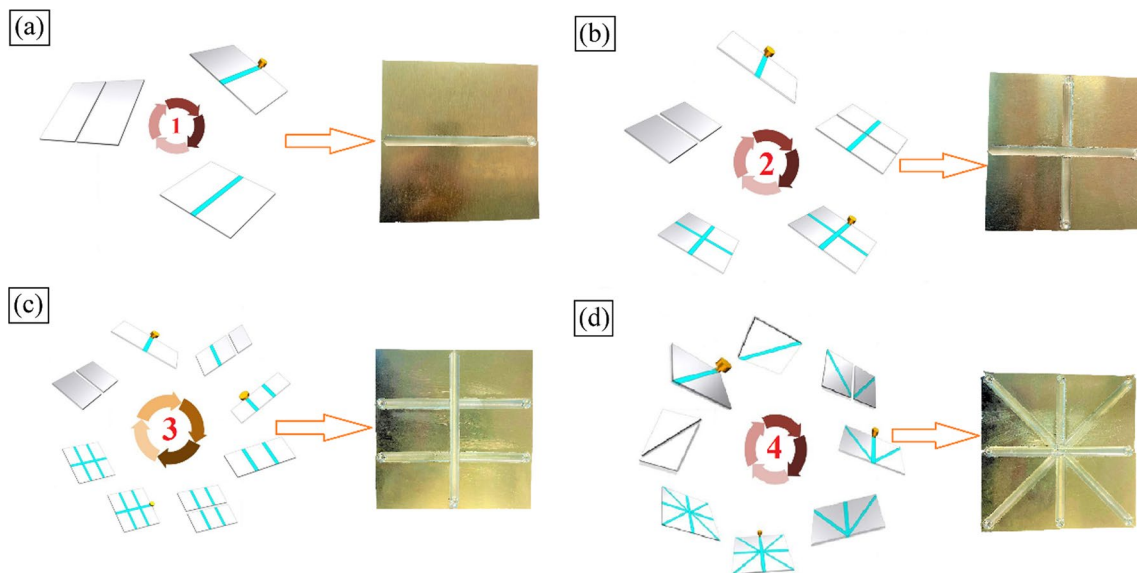
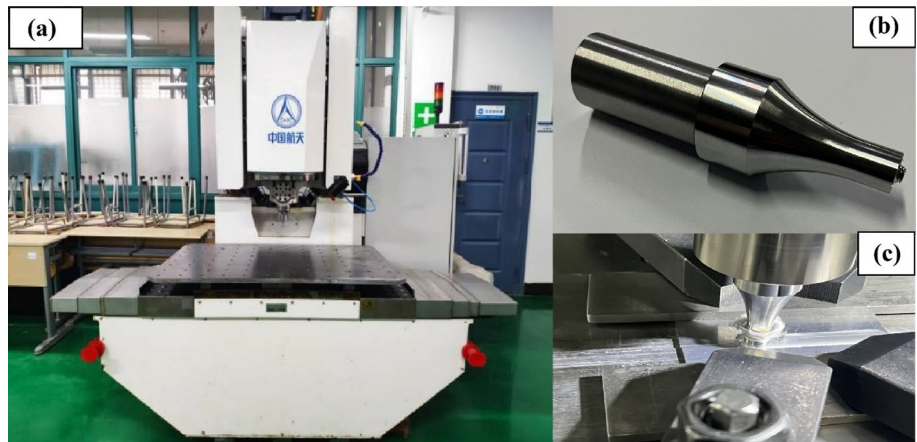


Fig. 2 Welding flow chart of the blank with: **a** the weld seam in a “–” shape, **b** the weld seams in a “+” shape **c** the weld seams in a “±” shape, **d** the weld seams in a “*” shape

Fig. 3 Spinning machine

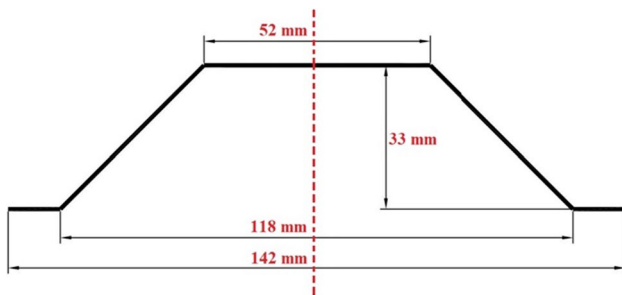
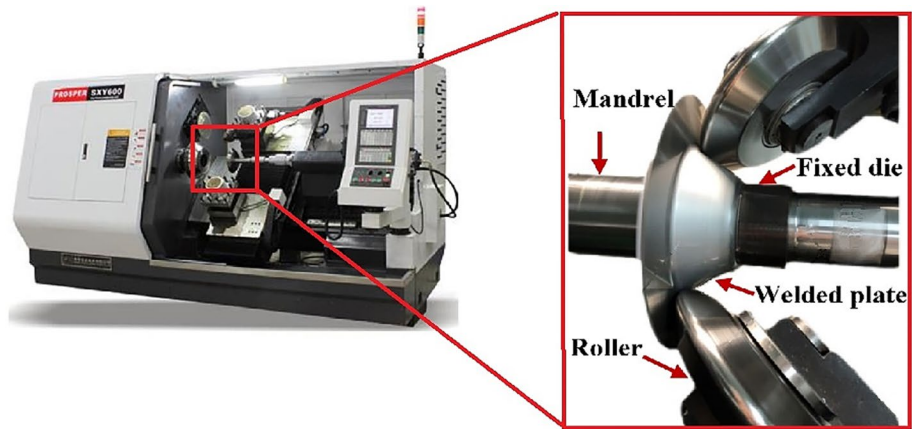


Fig. 4 Spinning workpiece cross-section

were then joined to form two 160 mm × 80 mm rectangular blanks, which were subsequently welded into a single 160 mm × 160 mm square blank with weld seams in a “✱” shape.

Prior to the spinning experiment, the square TWBs were transformed into round blanks with a diameter of 140 mm. Then they were sequentially spun using the SXY600 spinning machine, manufactured by Bosai Company, with a universal mandrel, as illustrated in Fig. 3. The spinning wheel operated at a feed speed of 50 mm/min and a spindle speed of 400 rpm. The spinning process employed a double spinning wheel, set at a 45° installation angle with a 4 mm radius. A conical workpiece with a forming angle of 45° was achieved through single-pass spinning. The dimensions of the resulting workpiece are detailed in Fig. 4.

The blank subjected to a single FSW (as shown in Fig. 2a) was cut along the direction perpendicular to the weld, and the microstructure at the weld was observed using an optical microscope. In addition, the microhardness change in the width direction of the weld was tested using a microhardness tester (Model: FM-700). Using wire cutting, the base metal and the blank after a single FSW were cut along the vertical weld direction to obtain the dog-bone-shaped tensile specimens with the shape and size shown in Fig. 5, and the tensile test was performed on the tensile test machine

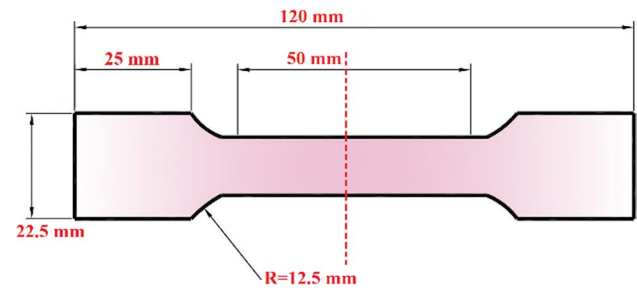


Fig. 5 Dimension of tensile specimen

(Model: WDW-50KN). The roughness meter (Model: TIME 3200) is used to measure the roughness of the weld position of the sheet metal after welding and the workpiece after spinning. Geomagic Control software was used to analyze the two-dimensional and three-dimensional accuracy of the formed workpiece. In addition, the workpiece cups after spinning are cut along the center weld and 1 cm away from the center weld, and the thickness of different positions is measured [24].

3 Results and Discussion

3.1 Mechanical Properties and Microhardness of Weld Area

Figure 6 illustrates the cross-sectional morphology of FSW joints, revealing a wider top and a narrower bottom in the entire weld area. The weld nugget zone (NZ) is situated at the center of the welded joint and experiences a high-temperature thermal cycle process. The temperature undergoes a step change during the welding process, with the highest temperature occurring near the NZ area, facilitating complete flow of the plastic metal. The thermo-mechanically affected zone (TMAZ) is situated at the edge of the NZ region, typically exhibiting good metal plasticity. As the



Fig. 6 Cross-section morphology of FSW joint

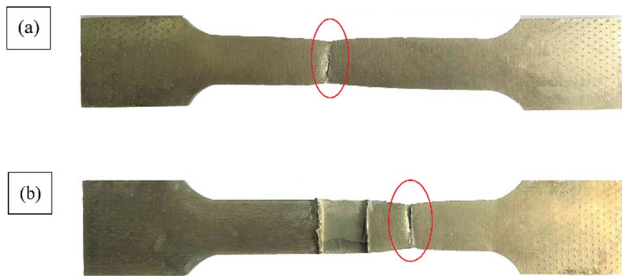


Fig. 7 Fracture of the tensile specimen from: **a** the base blank, **b** the weld blank

heat affected zone (HAZ) is distant from the NZ area, it experiences only the thermal cycle, which may lead to grain coarsening.

Figure 7a shows the fully annealed 2195 Al–Li alloy tensile specimen, with the fracture occurring at the center. Figure 7b shows the tensile specimen of 2195 Al–Li alloy after welding, with the fracture occurring in the base metal area distant from the weld zone. The reason for not breaking in the welding area is that the strength of the annealed 2195 alloy is low. FSW refines the grains in the welded joint area and improves the tensile strength of the welded area, resulting in that the fracture position of the tensile specimen after welding is not at the welded joint [25].

Figure 8 shows the tensile stress–strain curves of the fully annealed 2195 base metal and the welded blank. The tensile strength of the welded blank exceeds that of the base metal by approximately 20 MPa, while the elongation of the welded joint is lower compared to the base metal. The microhardness of the fully annealed 2195 aluminum–lithium alloy welded joints was measured, and the results are presented in Fig. 9. Hardness testing was conducted in the selected processing area, specifically the part with a shoulder diameter of 10 mm. The FM-700 microhardness tester was used to test the microhardness of the horizontal direction of the cross section of the sample by applying 200 g load to the test section and setting the residence time of 10 s and the step size of 0.6 mm. The microhardness of the welded joints surpasses that of the base metal, with the highest microhardness observed near the TMAZ adjacent to the NZ. The TMAZ undergoes changes in hardness due to the combined effects of heat and force. In contrast, the HAZ experiences

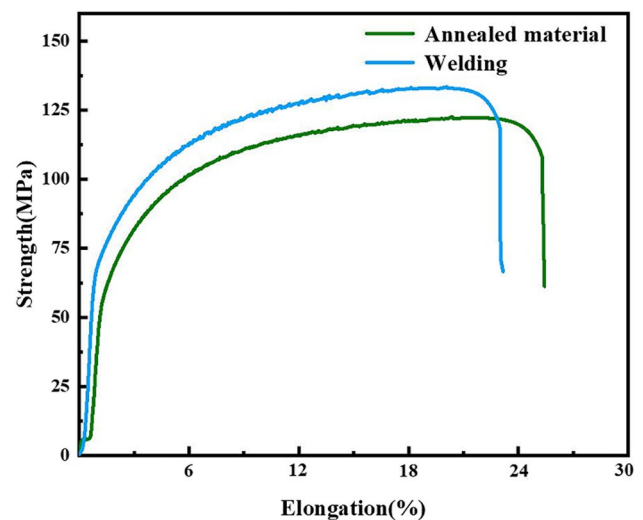


Fig. 8 Typical stress–strain curves of the weld joint, and the base metal

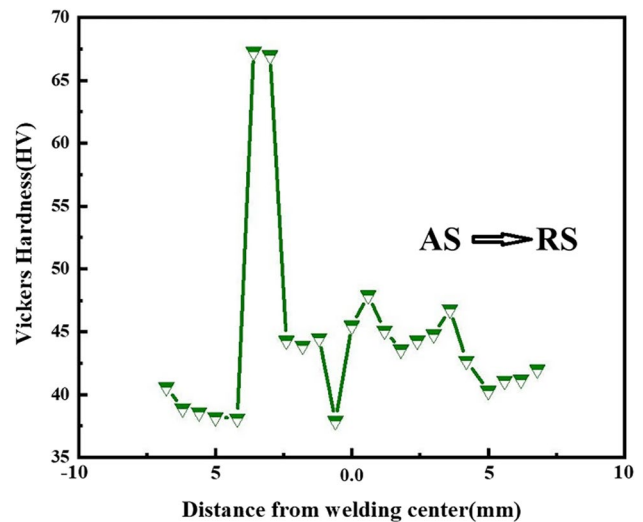


Fig. 9 Microhardness of welded joint

only thermal cycles, leading to grain growth and relatively lower microhardness.

The fracture surfaces of all specimens are recognized by the presence of voids. It has been known that the presence of a dimpled fracture surface shows the ductile fracture surface in metals [26, 27]. Figure 10 shows the tensile fracture morphology of the base metal and the welded blank. Figure 10a shows the tensile fracture morphology of the base metal, including an enlarged fracture diagram at a specific position. Similarly, Fig. 10b illustrates the tensile fracture morphology of the welded blank, along with an enlarged fracture diagram at a specific position. Due to the fracture position of the welded blank being distant from the weld area, the tensile fracture morphology observed in Fig. 10a and b

Fig. 10 Tensile fracture morphology: **a** the base metal **b** the welded blank

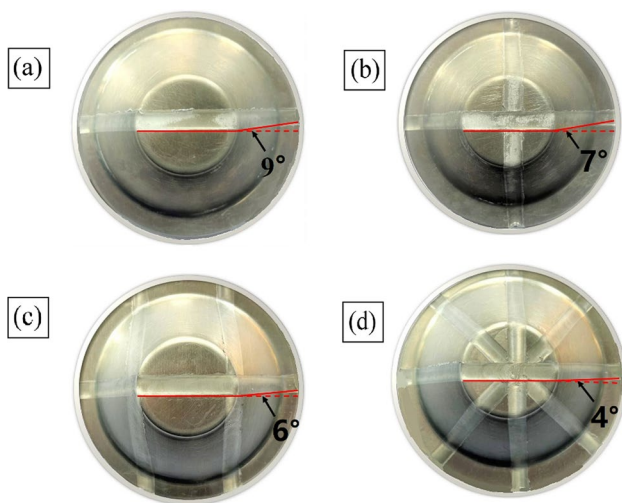
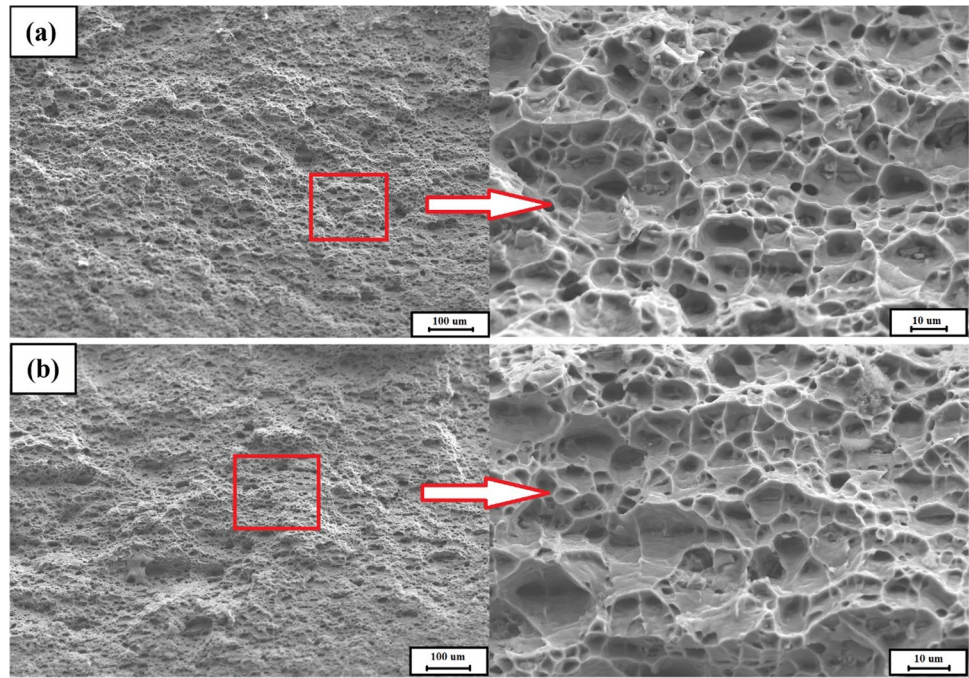


Fig. 11 Weld torsion in each spun workpiece with: **a** the weld seam in the “-” shape **b** the weld seams in the “+” shape **c** the weld seams in the “⊕” shape **d** the weld seams in the “⊗” shape

exhibits similarities. The tensile fracture displays extensive large and deep equiaxed dimples, along with tearing edges, indicating the excellent plasticity and confirming a ductile fracture mechanism.

3.2 The Weld Torsion Angles

Figure 11 shows the torsion angles of the welds of each spun workpiece. Figure 11a shows the weld torsion angle of the first type of tailor-welded spinning workpiece, which

measures 9° . Similarly, Fig. 11b shows the weld torsion angle of the second type of tailor-welded workpiece, measuring 7° . Furthermore, Fig. 11c shows the weld torsion angle of the third type of tailor-welded workpiece, measuring 6° , while Fig. 11d shows the weld torsion angle of the fourth type of tailor-welded workpiece, measuring 4° . As the number of welds increases, the torsion angle decreases gradually. In the spinning process of TWBs, the weld seam twists in accordance with the rotation of the spindle, with the torsion direction of the weld aligning consistently with the spindle's rotation direction [21].

3.3 The Surface Morphology

The surface morphology of both the weld and non-weld areas was observed before and after spinning. The surface roughness was measured within the rectangular area depicted in the figure, and the resulting roughness curve is shown in Fig. 12. Figure 12a shows the surface morphology of the weld area of the blank before spinning, along with the corresponding measured roughness curve. Similarly, Fig. 12b exhibits the surface morphology of the non-welded area of the blank before spinning, accompanied by the measured roughness curve. Furthermore, Fig. 12c shows the surface morphology of the weld area of the workpiece after spinning, together with the measured roughness curve. Finally, Fig. 12d presents the surface morphology of the non-welded area of the workpiece after spinning, along with the measured roughness curve. The spinning process can effectively reduce the surface roughness of the weld area by decreasing the height of the protruding portion of the

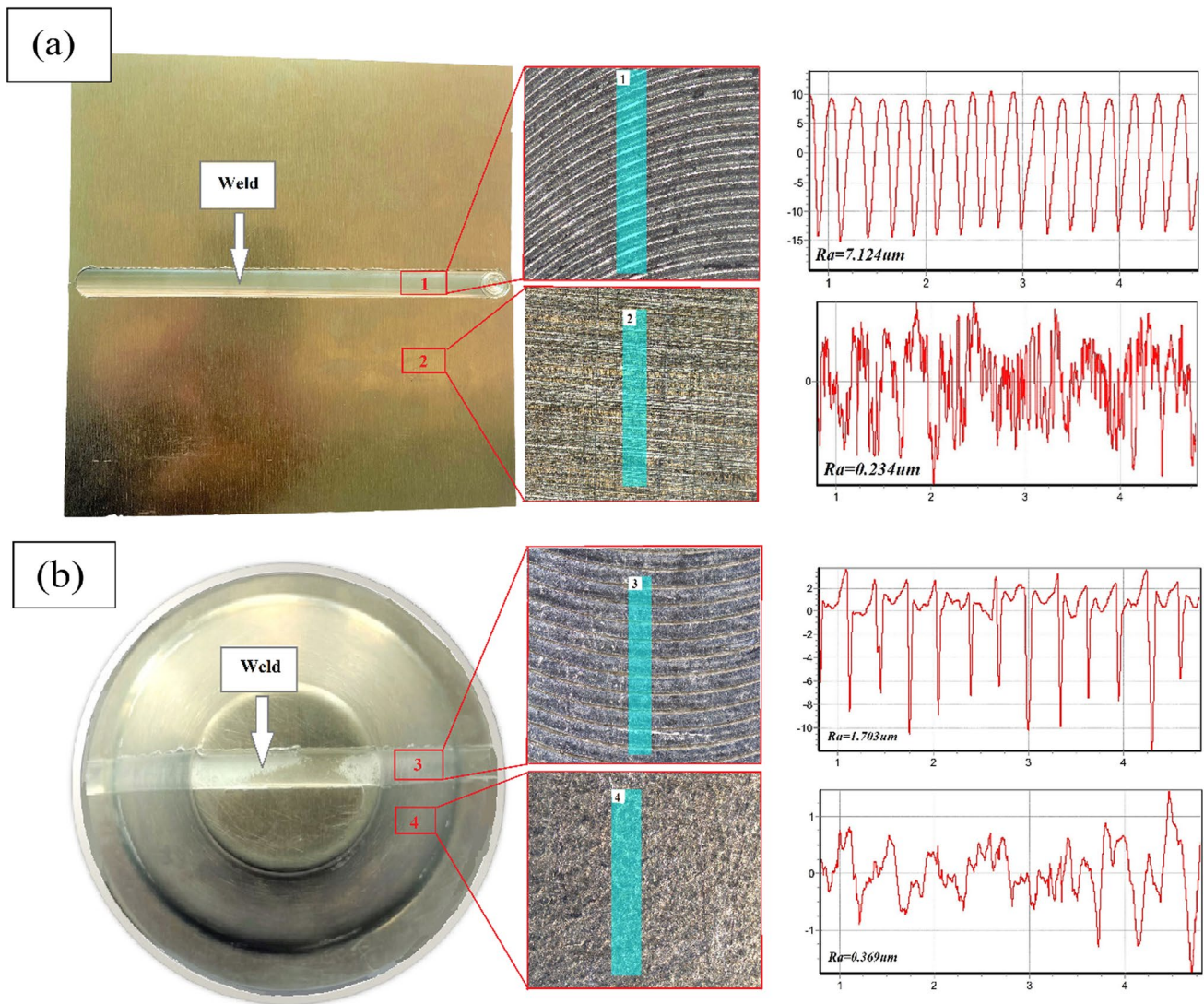


Fig. 12 Surface morphology and the roughness curve: **a** the weld blank **b** the spun workpiece

welding texture. Conversely, in the non-welded area, the surface roughness of the workpiece is slightly improved after spinning.

3.4 The Thickness Variation

Figure 13 shows the thickness variations between the weld area and non-weld area of each spun workpiece. Figure 13a shows the thickness variation of the workpiece with the “-” shaped weld seam. Due to the pressing action of the stirring head, the weld area exhibits a thinner thickness compared to the non-weld area. The minimum thickness is at the weld seam area, measuring 1.2 mm. Figure 13b the thickness variation in the workpiece with the “+” shaped weld seam, where the thinning pattern is consistent with that observed in Fig. 13a. In this case, the region where the welds overlap

experiences further thinning. Figure 13c and d represent the thickness variations of the “+” and “*” weld seam workpieces, respectively. As observed, similar to Fig. 13a and b, the weld seam area has a thinner thickness compared to the non-weld seam area. Furthermore, the thickness of the overlapping weld seam is further reduced.

3.5 The 2D Accuracy and the 3D Accuracy

Figure 14 shows the 2D accuracy of each spun workpiece. Figure 14a shows the 2D accuracy of the weld seam in the “-” shape spinning workpiece, denoted as D , which represents the deviation between the contour of the workpiece and the theoretical contour. Initially, during the spinning stage, negative precision deviation is observed, reaching a maximum value of -0.7182 mm. In the final spinning

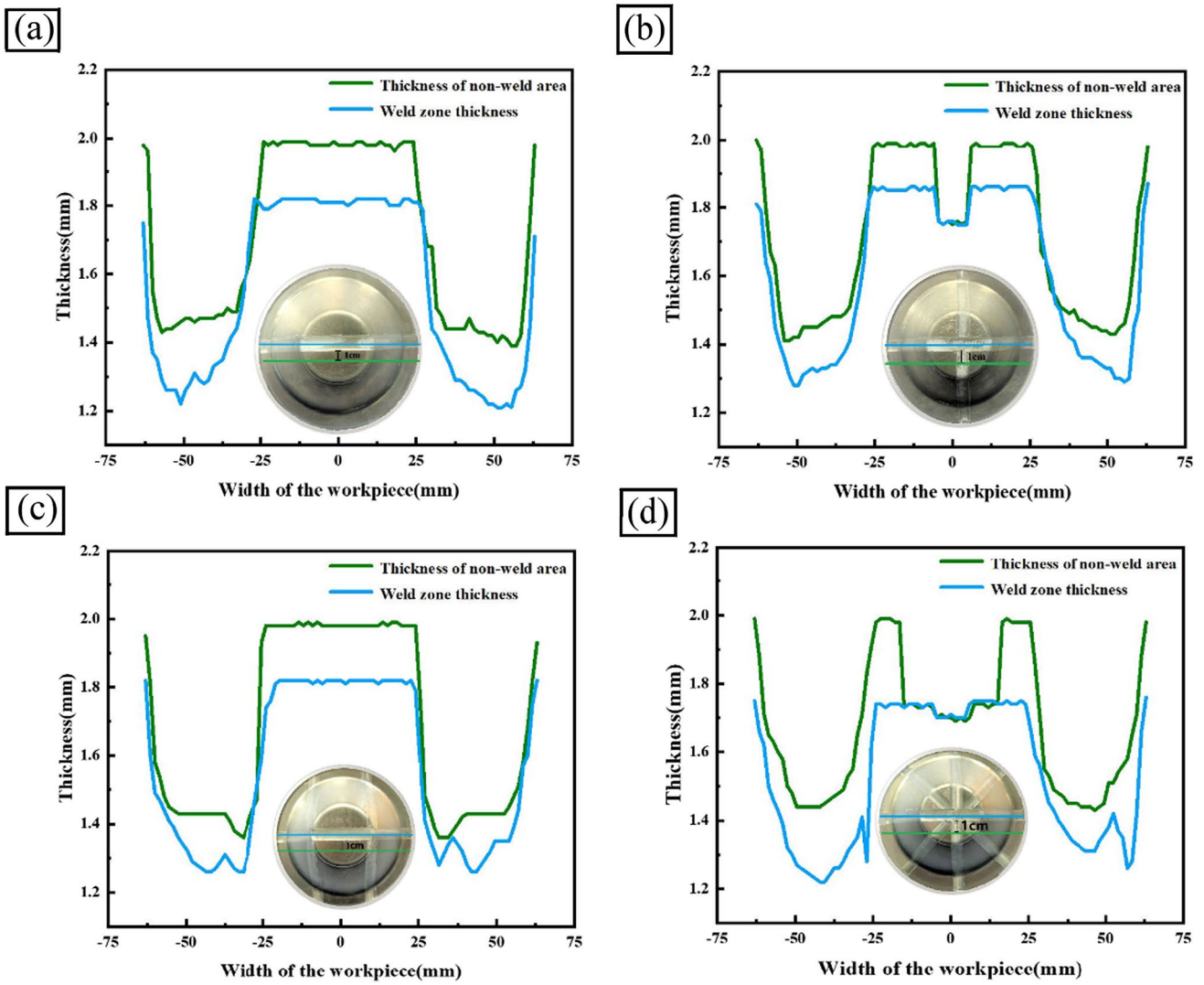


Fig. 13 The thickness variations of the weld area and non-weld area of each spun workpieces with **a** the weld seam in the “-” shape **b** the weld seams in the “+” shape **c** the weld seams in the “±” shape **d** the weld seams in the “*” shape workpiece

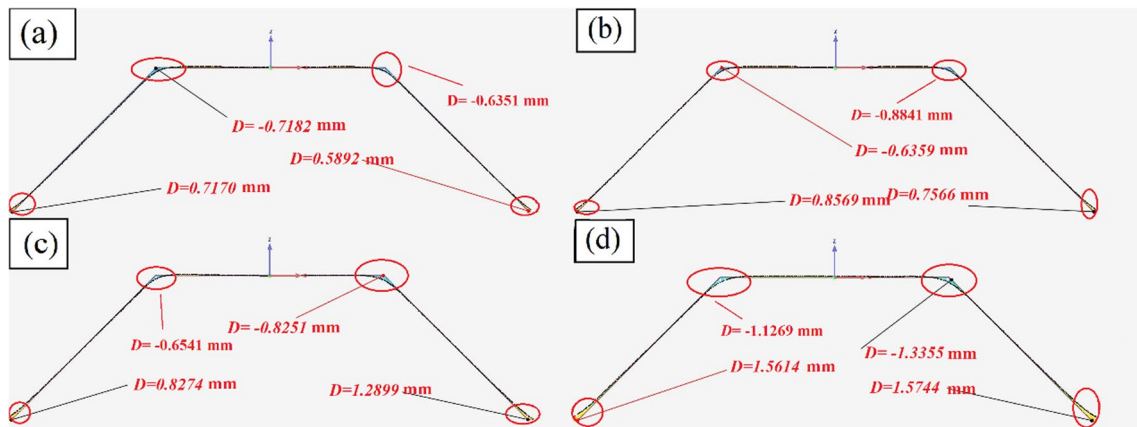
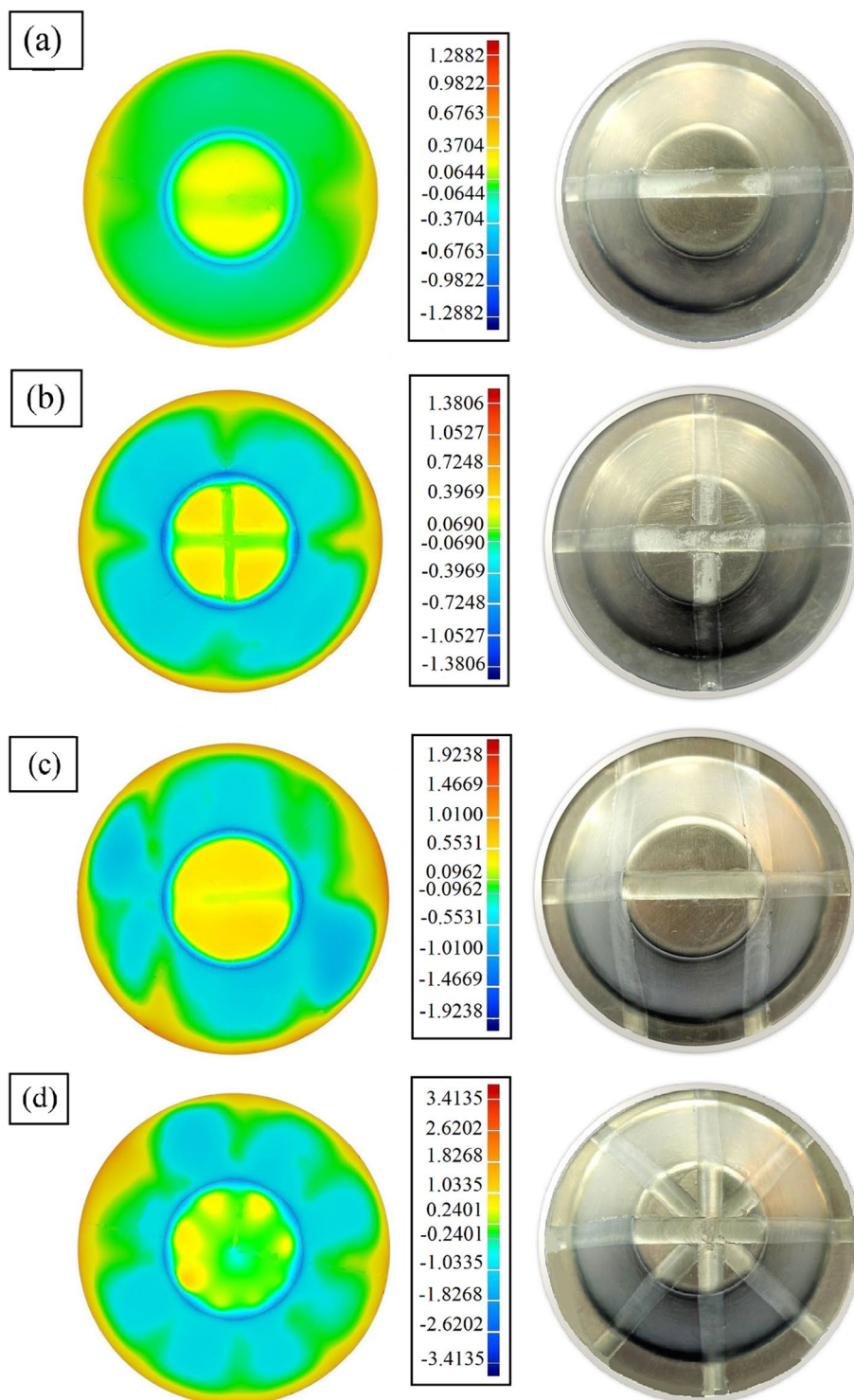


Fig. 14 2D accuracy of each spun workpiece with: **a** the weld seam in the “-” shape **b** the weld seams in the “+” shape **c** the weld seams in the “±” shape **d** the weld seams in the “*” shape

stage, a positive precision deviation occurs due to the influence of the flange edge, with a maximum deviation of 0.7170 mm. Figure 14b shows the 2D accuracy of the weld seams in the “+” shape spinning workpiece. Negative precision deviation is observed at the beginning of the spinning stage, with a maximum deviation of −0.6359 mm. In

the final spinning stage, a positive precision deviation is observed, reaching a maximum deviation of 0.8569 mm. Figure 14c shows the 2D accuracy of the weld seams in the “±” shape spinning workpiece. Negative precision deviation is observed at the beginning of the spinning stage, with a maximum deviation of −0.8251 mm. In

Fig. 15 3D accuracy of each workpiece with: **a** the weld seam in the “-” shape **b** the weld seams in the “+” shape **c** the weld seams in the “±” shape **d** the weld seams in the “✳” shape



the final spinning stage, a positive precision deviation is observed, reaching a maximum deviation of 1.2899 mm. Figure 14d shows the 2D accuracy of the weld seams in the “✱” shape spinning workpiece. Negative precision deviation is observed at the beginning of the spinning stage, with a maximum deviation of -1.3355 mm. In the final spinning stage, a positive precision deviation is observed, reaching a maximum deviation of 1.5744 mm. Workpieces produced using different weld seam distributions exhibit negative precision deviation at the start of spinning and positive precision deviation at the final spinning stage. As the number of welds increases, the forming accuracy of the spun workpiece gradually decreases.

Figure 15 shows the 3D accuracy of each spun workpiece. Figure 15a shows the 3D accuracy of the workpiece with the weld seam in the “-” shape, where the forming contour of the weld area closely matches the theoretical contour. The 3D accuracy plot reveals a negative accuracy deviation at the beginning of spinning and a positive accuracy deviation at the end of spinning, consistent with the 2D accuracy results. Figure 15b shows the 3D accuracy of the weld seams in the “+” shape workpiece, wherein the weld area exhibits slight uplift due to residual stress after spinning, leading to a positive precision deviation. Figure 15c showcases the 3D accuracy of the weld seams in the “≠” shape workpiece. The weld area exhibits a positive precision deviation, indicating a distinct distribution and trend of welds. In the initial spinning stage, a significant negative precision deviation is observed, while the final spinning stage results in slight warping of the TWBs, leading to a positive precision deviation. Figure 15d shows the 3D accuracy of the weld seams in the “✱” shape workpiece, where the accuracy of the weld area demonstrates evident orientation and distribution. At the onset of spinning, a negative precision deviation is present, which transitions into a substantial positive precision deviation towards the end of spinning due to the influence of the flange edge. The 3D accuracy plot reveals that an increasing number of welds deteriorates the accuracy of the spun workpiece, accompanied by a slight uplift in the weld area, resulting in a minor positive accuracy deviation from the theoretical workpiece contour.

4 Conclusion

This study aims to investigate the influence of the weld seam distribution of TWBs by FSW on spin forming. From the results obtained in this investigation, the following conclusions can be drawn:

1. In the case of the fully annealed 2195 Al–Li alloy, the tensile strength of the weld zone exceeds that of the base metal and the highest hardness is observed in the TMAZ located on the advancing side of the weld area.
2. Spinning processing offers the capability to decrease the surface roughness of the weld area. However, in the non-welded area, the surface roughness of the workpiece after spinning experiences a slight increase compared to its weld state.
3. In spinning, the weld seam undergoes twisting in alignment with the spindle rotation. The torsion direction of the weld aligns with the rotation direction of the spindle. The weld torsion angle of the spun workpiece gradually decreases as the number of welds increases.
4. Each spun workpiece exhibits a phenomenon where the thickness of the weld area is thinner than the non-welded area, and the overlapping of weld seams further exacerbates the thinning of the thickness.
5. The accuracy scanning results reveal a slight bulge in the weld area of each spun workpiece. With the increase of the number of welds, the accuracy of the spun workpiece is reduced. The precision deviation occurs at the beginning and end of spinning.

Acknowledgements The National Natural Science Foundation of China (Grant No. 52301090); Shandong Province ZR2023QE275 provided research facilities for this work; Shandong Province 2019GGX102023 key research and development plan project.

References

1. Xing, L., Zhan, M., Gao, P. F., & Ma, F. (2018). A method for establishing a continuous constitutive model of welded metals. *Materials Science and Engineering: A*, 718, 228–240. <https://doi.org/10.1016/j.msea.2018.01.062>
2. Ma, F., Gao, P. F., Ma, P. Y., & Zhan, M. (2019). Power spinning of the curved head with tailor welded aluminum alloy blank: Deformation, microstructure, and property. *Metals*, 9(12), 1359. <https://doi.org/10.3390/met9121359>
3. Zhan, M., Wang, X. X., & Long, H. (2016). Mechanism of grain refinement of aluminium alloy in shear spinning under different deviation ratios. *Materials and Design*, 108, 207–216. <https://doi.org/10.1016/j.matdes.2016.06.095>
4. Xia, Q. X., Xiao, G. F., Long, H., Cheng, X. Q., & Sheng, X. F. (2014). A review of process advancement of novel metal spinning. *International Journal of Machine Tools and Manufacture*, 85, 100–121. <https://doi.org/10.1016/j.ijmactools.2014.05.005>
5. Gan, T., Yu, Z. Q., Zhao, Y. X., Evsyukov, S. A., & Lai, X. M. (2018). Effects of backward path parameters on formability in conventional spinning of aluminum hemispherical parts. *Transactions of Nonferrous Metals Society of China*, 28, 328–339. [https://doi.org/10.1016/S1003-6326\(18\)64666-7](https://doi.org/10.1016/S1003-6326(18)64666-7)
6. Chaskis, S., Stachouli, E., Gavalas, E., Bouzouni, M., & Papaefthymiou, S. (2022). Microstructure, phase formation and heat-treating of novel cast Al–Mg–Zn–Cu–Si lightweight complex concentrated aluminum based alloy. *Materials*, 15(9), 3169. <https://doi.org/10.3390/ma15093169>

7. Gözde, A., Onur, A., & Bülent, B. (2021). Characterization of Al-7075/T651 alloy by RRA heat treatment and different pre-deformation effects. *Transactions of the Indian Institute of Metals*, 74(12), 3025–3033. <https://doi.org/10.1007/s12666-021-02369-5>
8. Gözde, A., Abbas, T. Ö., & Bülent, B. (2023). A survey of the effect of cryogenic treatment and natural ageing on structural changes and second-phase precipitation in Al–Zn–Mg–Cu alloy. *Journal of Thermal Analysis and Calorimetry*, 148, 10713–10725. <https://doi.org/10.1007/s10973-023-12414-8>
9. Gözde, A., & Bülent, B. (2022). Metallurgical characterization of natural aging effects on pre-deformed Al 7075/T651 alloy during retrogression and re-aging heat treatment. *Kovove Materialy-Metallic Materials*, 60, 209–222. <https://doi.org/10.31577/km.2022.4.209>
10. Zhang, J., Feng, X. S., Gao, J. S., Huang, H., Ma, Z. Q., & Guo, L. J. (2018). Effects of welding parameters and post-heat treatment on mechanical properties of friction stir welded AA2195-T8 Al–Li alloy. *Journal of Materials Science and Technology*, 34, 219–227. <https://doi.org/10.1016/j.jmst.2017.11.033>
11. Tao, Y., Zhang, Z., Xue, P., Ni, D. R., Xiao, B. L., & Ma, Z. Y. (2022). Effect of post weld artificial aging and water cooling on microstructure and mechanical properties of friction stir welded 2198-T8 Al–Li joints. *Journal of Materials Science and Technology*, 123, 92–112. <https://doi.org/10.1016/j.jmst.2022.01.020>
12. Amin, A., Behrouz, B., Mahmoud, A., Farzaneh, S., Seyyed, E. M., & Ahmad, O. M. (2021). A modified version of friction stirwelding process of aluminum alloys: Analyzing the thermal treatment and wear behavior. *Proceedings of the Institution of Mechanical Engineers, Part L: Journal of Materials: Design and Applications*, 30(1), 1–19. <https://doi.org/10.1177/14644207211023987>
13. Behrouz, B., Mahmoud, A., & Reza, H. (2020). Comparison of different welding methods on mechanical properties and formability behaviors of tailor welded blanks (TWB) made from AA6061 alloys. *Proceedings of the Institution of Mechanical Engineers, Part C: Journal of Mechanical Engineering Science*, 30(1), 1–13. <https://doi.org/10.1177/0954406220952504>
14. Mahmoud, A., Amin, A., Behrouz, B., Ahmad, O. M., Farzaneh, S., & Mostafa, D. (2021). Study on the effect of the welding environment on the dynamic recrystallization phenomenon and residual stresses during the friction stir welding process of aluminum alloy. *Proceedings of the Institution of Mechanical Engineers, Part L: Journal of Materials: Design and Applications*, 235(8), 1809–1826. <https://doi.org/10.1177/14644207211025113>
15. Hammood, A. S., Esmailzadeh, M., Hosseini, S. N., Karimi, S., Calliari, I., Pezzato, L., & Brittain, R. (2023). Effect of friction stir welding parameters on microstructure and corrosion behavior of 2101 duplex stainless steel in simulated body fluid. *International Journal of Precision Engineering and Manufacturing-Green Technology*, 10, 327–337. <https://doi.org/10.1007/s40684-022-00440-0>
16. Laska, A., Szkodo, M., Pawłowski, Ł., & Gajowiec, G. (2023). Corrosion properties of dissimilar AA6082/AA6060 friction stir welded butt joints in different NaCl concentrations. *International Journal of Precision Engineering and Manufacturing-Green Technology*, 10, 457–477. <https://doi.org/10.1007/s40684-022-00441-z>
17. Lin, Y. C., Chen, J. Y., He, D. G., & Li, X. H. (2020). MarginAl-restraint mandrel-free spinning process for thin-walled ellipsoidal heads. *Advances in Manufacturing*, 8, 189–203. <https://doi.org/10.1007/s40436-020-00296-0>
18. Yan, X. G., Zhan, M., Wang, Y., Gao, P. F., & Wang, Y. D. (2023). Criterion and processing-dependence of forming states in the die-less spinning of conical part. *The International Journal of Advanced Manufacturing Technology*, 125, 3037–3051. <https://doi.org/10.1007/s00170-023-10867-7>
19. Zhou, S. Y., Han, Z. R., Jia, Z., Liu, B. M., & Gong, X. (2023). Research on the wall thinning influencing factors in die-less spinning by hemisphere roller. *The International Journal of Advanced Manufacturing Technology*, 126, 2497–2508. <https://doi.org/10.1007/s00170-023-11296-2>
20. Izadpanah, S., & Amini, M. (2023). Application of computationally advanced 3D finite element simulation for stress and strain Analysis of single and multi-pass spinning processes with experimental validation. *International Journal of Precision Engineering and Manufacturing*, 24, 1335–1353. <https://doi.org/10.1007/s12541-023-00821-8>
21. Zhang, H. R., Zhan, M., Zheng, Z. B., & Li, R. (2022). Manufacture of thin-walled axisymmetric components by friction stir welding and spinning of Al–Li alloy. *JOM Journal of the Minerals Metals and Materials Society*, 74, 3248–3260. <https://doi.org/10.1007/s11837-022-05394-x>
22. Zhang, H. R., Zhan, M., Zheng, Z. B., & Li, R. (2021). A systematic study on the effects of process parameters on spinning of thin-walled curved surface parts with 2195 Al–Li alloy tailor welded blanks produced by FSW. *Frontiers in Materials*, 8, 809018. <https://doi.org/10.3389/fmats.2021.809018>
23. Zhang, H. R., Zhan, M., Zheng, F. B., Li, R., & Ma, F. (2022). Forming dependence on spin roller paths for thin-walled complex components from 2195 Al–Li alloy TWBs. *The International Journal of Advanced Manufacturing Technology*, 120, 3113–3122. <https://doi.org/10.1007/s00170-022-08974-y>
24. Lakshminarayanan, A. K., Malarvizhi, S., & Balasubramanian, V. (2012). Developing friction stir welding window for AA2219 aluminium alloy. *Transactions of Nonferrous Metals Society of China*, 21, 2339–2347. [https://doi.org/10.1016/S1003-6326\(11\)61018-2](https://doi.org/10.1016/S1003-6326(11)61018-2)
25. Moreira, P., Jesus, D. A., Figueiredo, D. M., Windisch, M., Sinnema, G., & Castro, D. P. (2012). Fatigue and fracture behaviour of friction stir welded aluminium–lithium 2195. *Theoretical and Applied Fracture Mechanics*, 60(1), 1–9. <https://doi.org/10.1016/j.tafmec.2012.06.001>
26. Mahmoud, A., Behrouz, B., Amin, A., & Ahmad, O. M. (2021). Different attempt to improve the formability of aluminum tailor welded blanks (TWB) produced by the FSW. *International Journal of Material Forming*, 14, 1189–1208. <https://doi.org/10.1007/s12289-021-01632-w>
27. Amin, A., Behrouz, B., Mahmoud, A., Amir, H. K., & Ahmad, O. M. (2021). Comparison of the weldability of AA6061-T6 joint under different friction stir welding conditions. *Journal of Materials Engineering and Performance*, 30, 1110–1127. <https://doi.org/10.1007/s11665-020-05379-4>

Publisher's Note Springer Nature remains neutral with regard to jurisdictional claims in published maps and institutional affiliations.

Springer Nature or its licensor (e.g. a society or other partner) holds exclusive rights to this article under a publishing agreement with the author(s) or other rightsholder(s); author self-archiving of the accepted manuscript version of this article is solely governed by the terms of such publishing agreement and applicable law.



Shouyi Sun is a postgraduate student at the School of Mechanical and Automotive Engineering, Qingdao University of Technology, China. His main research interest is aluminum alloy friction stir welding and spin forming.



Gaowei Cao is a postgraduate student at the School of Mechanical and Automotive Engineering, Qingdao University of Technology, China. His main research interest is aluminum alloy friction stir welding.



Jin Wang is a professor in the School of Mechanical and Automotive Engineering at Qingdao University of Technology, China. His research interests are focused on metal forming and friction stir welding.



Shuai Zhang is a postgraduate student at the School of Mechanical and Automotive Engineering, Qingdao University of Technology, China. His research interests include friction stir processing, electrochemical hydrogen evolution of pure copper catalysts, and thermal processing of materials.



Bo Gao received his PhD degree (2022) in the State Key Laboratory for Mechanical Behavior of Materials at Xi'an Jiaotong University in China. He is currently a lecturer in the School of Mechanical and Automotive Engineering at Qingdao University of Technology. His research interests are focused on engineering nanocrystals and 2D materials for catalysis, functional films for energy conversion.